Identifying Majorana vortex modes via nonlocal transport

Björn Sbierski,[1,2] Max Geier,[3] An-Ping Li,[4] Matthew Brahlek,[5]
Robert G. Moore,[5] and Joel E. Moore[1,6]

[1]*Department of Physics, University of California, Berkeley, California 94720, USA*
[2]*Department of Physics and Arnold Sommerfeld Center for Theoretical Physics, Ludwig-Maximilians-Universität München, Theresienstr. 37, D-80333 München, Germany*
[3]*Center for Quantum Devices, Niels Bohr Institute, University of Copenhagen, DK-2100 Copenhagen, Denmark*
[4]*Center for Nanophase Materials Sciences, Oak Ridge National Laboratory, Oak Ridge, Tennessee 37831, USA*
[5]*Materials Sciences and Technology Division, Oak Ridge National Laboratory, Oak Ridge, Tennessee 37831, USA*
[6]*Materials Sciences Division, Lawrence Berkeley National Laboratory, Berkeley, California 94720, USA*

(Received 2 August 2021; revised 7 June 2022; accepted 27 June 2022; published 14 July 2022)

The combination of two-dimensional Dirac surface states with *s*-wave superconductivity is expected to generate localized topological Majorana zero modes in vortex cores. Putative experimental signatures of these modes have been reported for heterostructures of proximitized topological insulators, iron-based superconductors or certain transition metal dichalcogenides. Despite these efforts, the Majorana nature of the observed excitation is still under debate. We propose to identify the presence of Majorana vortex modes using a nonlocal transport measurement protocol originally employed for one-dimensional settings. In the case of an isolated subgap state, the protocol provides a spatial map of the ratio of local charge- and probability-density which offers a clear distinction between Majorana and ordinary fermionic modes. We show that these distinctive features survive in the experimentally relevant case of hybridizing vortex core modes.

DOI: 10.1103/PhysRevB.106.035413

I. INTRODUCTION

In condensed matter physics, Majorana zero energy modes are highly sought after subgap states localized in topological superconductors and certain fractional quantum Hall states [1,2]. Whereas initial efforts were mainly directed towards one-dimensional systems based on semiconductor quantum wires in proximity with conventional superconductors ("Majorana" wire) [3], recent progress in this direction has been slowed by the ambiguity related to the interpretation of transport measurements [4] local to the ends of the wire. As a consequence, it has been proposed that nonlocal transport setups can give a much cleaner picture of the nature of subgap states [5–8] with a small number of recent experiments already available [9,10].

Candidate systems for Majorana zero modes are not limited to one spatial dimension. In a classic paper [11], Fu and Kane proposed to realize Majorana zero modes in the center of a vortex in the superconducting order parameter assuming the latter pairs a single-species of two-dimensional Dirac quasiparticles. The resulting zero-energy excitations are also known as Majorana vortex modes (MVM). The initial proposal was framed in the context of topological insulator surface states proximitized to a superconducting layer, which was subsequently realized in experiment [12,13]. However the unambiguous identification of MVM in the experimentally observed local density of states (LDOS) is complicated by the fact that the putative MVM at $E_0 = 0$ is by far not the only subgap state localized at the vortex position. In addition, theory predicts a whole ladder of finite-energy Caroli-de Gennes-Matricon (CdGM) states, with $E_m = m\Delta_0^2/\mu,\ \ m = 0, \pm 1, \pm 2, \ldots$ [14–17] where Δ_0 is the pairing far away from any vortices and μ is the chemical potential. The detection of energetically isolated MVMs at $E_0 = 0$ requires $E_1 = \Delta_0^2/\mu$ to exceed the experimental energy resolution.

Recently, progress in this direction was made in a variety of novel "Fu-Kane" materials that combine bulk superconductivity with two-dimensional surface Dirac states of topological origin and feature E_1 on the order of a few hundred μeV. Prominent example materials with claims for MVM based on LDOS measurements are the iron-based superconductors $FeTe_{0.55}Se_{0.45}$ [17–22], $(Li_{0.84}Fe_{0.16})OHFeSe$ [23,24], LiFeAs [25], $CaKFe_4As_4$ [26] or the transition metal dichalcogenide $2M - WS_2$ [27,28]. Besides the agreement of the observed energy spacings with the above theory, another point consistent with the existence of MVMs is the nonoscillatory radial profile of the MVM-LDOS [24].

On the other hand, for the same sample of $FeTe_{0.55}Se_{0.45}$, a coexistence of topological vortices and trivial vortices (with CdGM spectra in accordance with $m = \pm\frac{1}{2}, \pm\frac{3}{2}, \ldots$) has been reported [17]. A possible explanation is a high sensitivity of the surface topological superconducting phase to the exact stoichiometric composition and local chemical potential [20,21,29]. There are other concerns regarding the MVM interpretation of experimental results in the putative Fu-Kane materials. They include the possible trivial origin of a non-split zero-energy vortex bound state [30], the sensitivity of

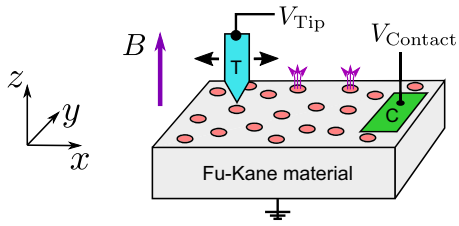

FIG. 1. Schematic of the proposed nonlocal transport setup for a Fu-Kane material with superconducting surface Dirac state in the vortex phase. In addition to the standard scanning-tunneling spectroscopy setup using grounded bulk and tip contact ("T"), an additional contact ("C") is required. This contact does not need to be realized as a second tip but can be spatially extended.

the vortex subgap state's energy spacings to the pairing profile $\Delta(r)$ and to impurities [31], or the lack of a robustly quantized conductance plateau in a strong-coupling transport experiment [32].

In this work we propose a framework to identify the presence (or absence) of MVMs in the two-dimensional platform using ideas of nonlocal transport first developed for one-dimensional superconducting heterostructures [6]. In particular, we propose to use a non-local transport measurement to spatially map the ratio $[q/n](\mathbf{r})$ of local charge density (q) and probability-density (n) of subgap wave functions at various energies. We discuss how the data reveals telltale signatures of either topological MVM or ordinary CdGM states. In contrast to a closely related pioneering experiment on a one-dimensional quantum wire [9], the application of the proposed technique to realistic vortex modes comes with a number of important modifications: In the one-dimensional wire case, the spatial resolution is usually limited to the positions of the tunneling contacts at the two ends of the wire as STM is not applicable. In the two-dimensional case at least one of the two required surface contacts can be realized as a movable STM tip (see "T" in Fig. 1), which is sufficient to achieve a spatially resolved q/n. The second contact ("C") can be another STM tip [33–35], if available, or any other extended type of electrical contact like a patterned metallic overlayer or a graphene flake.

A second important difference pertains to the complexity of the electronic system: While an ideal one-dimensional topological superconductor harbors two Majorana zero modes at its ends, the two-dimensional situation is characterized by the fact that vortices (and their putative MVMs) are located in a disordered lattice with local but essentially random hybridizations [36,37] that modify the spectrum from the case of a uniform lattice [38,39]. Although we start discussing the most simple case of a single vortex-pair analytically, we then take into account experimental reality with many vortices using extensive numerical simulations based on a tight-binding model of the Dirac Hamiltonian.

The rest of the paper is organized as follows: In Sec. II we present the low-energy two-dimensional Fu-Kane model and its tight-binding approximation. We then review the description of nonlocal superconducting quantum transport in Sec. III. The case of a single vortex pair is treated in Sec. IV which is suitable to present our protocol proposed for experiments. The applicability of our main ideas to a realistic disordered vortex lattice is demonstrated in Sec. V and a conclusion is contained in Sec. VI.

II. MODEL AND VORTEX MODES

We consider a single two-dimensional Dirac surface Hamiltonian $\mathcal{H}_0 = -i\hbar v[\sigma_x\partial_x + \sigma_y\partial_y] - \mu$ with velocity v, chemical potential μ and the σ-Pauli matrices acting in spin space [40]. The second-quantized s-wave pairing Hamiltonian reads [11,36,37]

$$H_{BCS} = \int_{\mathbf{r}} \psi_{\mathbf{r}}^\dagger \mathcal{H}_0 \psi_{\mathbf{r}} + \Delta\psi_{\mathbf{r},\uparrow}^\dagger \psi_{\mathbf{r},\downarrow}^\dagger + \Delta^* \psi_{\mathbf{r},\downarrow}\psi_{\mathbf{r},\uparrow}, \quad (1)$$

where Δ is the pairing field and the spinor of electronic annihilation operators is given by $\psi_{\mathbf{r}} = (\psi_{\uparrow,\mathbf{r}}, \psi_{\downarrow,\mathbf{r}})^{\mathrm{T}}$. The ansatz $\psi_{\mathbf{r},\sigma} \equiv \sum_n u_{\sigma,n}(\mathbf{r})\gamma_n + v_{\sigma,n}^*(\mathbf{r})\gamma_n^\dagger$ leads to the following Bogoliubov–de Gennes (BdG) equations for eigenmodes γ_n and -energies E_n,

$$\mathcal{H}_{BdG}\Phi(\mathbf{r}) = E_n\Phi(\mathbf{r}) \quad (2)$$

$$\mathcal{H}_{BdG} = \tau_z(v[\sigma_x p_x + \sigma_y p_y] - \mu) + \tau_x \mathrm{Re}\Delta - \tau_y \mathrm{Im}\Delta \quad (3)$$

with $\Phi^{\mathrm{T}}(\mathbf{r}) = (u_\uparrow, u_\downarrow, v_\downarrow, -v_\uparrow)$ and Pauli matrices τ_μ acting in particle-hole space. The particle-hole symmetry is $\mathcal{P} = \sigma_y\tau_y\mathcal{K}$ with $\mathcal{P}^2 = +1$ and $\mathcal{K}$ complex conjugation. In the homogeneous case, the energies for momentum $\mathbf{k}$ are given by $E_{\mathbf{k}} = \pm(\Delta^2 + (\pm vk - \mu)^2)^{1/2}$.

A magnetic field B_z applied orthogonal to the surface creates vortices in the pairing field [41],

$$\Delta(\mathbf{r}) = \Delta_0 \prod_j f(|\mathbf{r} - \mathbf{R}_j|)\frac{(x - x_j) + i(y - y_j)}{|\mathbf{r} - \mathbf{R}_j|} \quad (4)$$

with $\mathbf{R}_j = x_j\mathbf{e}_{\mathbf{x}} + y_j\mathbf{e}_{\mathbf{y}}$ the vortex positions and the function $f(r) = \tanh(r/\xi)$ modeling the decay of the pairing amplitude from its bulk value Δ_0 towards the vortex core within lengthscale ξ. For a single vortex at the origin, Eq. (4) reduces to the simple polar-coordinate expression $\Delta(r,\phi) = \Delta_0 f(r)e^{i\phi}$. The magnetic field can be found from the solution of the London equation which, for the single vortex case, reads $B_z(r) = \frac{\Phi_0}{2\pi\lambda^2}K_0(r/\lambda)$ with corresponding vector potential $\mathbf{A}(\mathbf{r}) = \mathbf{e}_\phi\frac{\Phi_0}{2\pi r}[1 - \frac{r}{\lambda}K_1(r/\lambda)]$ in the London gauge. Here, $\Phi_0 = \pi\hbar/e$ is the magnetic flux quantum piercing the vortex while the radial decay of $B_z(r)$ is controlled by the London penetration depth λ. The modified Bessel function of the second kind is denoted by $K_l(x)$. The vector potential enters in the Hamiltonian via the replacement $\mathbf{p} \to \mathbf{p} - \tau_z e\mathbf{A}(\mathbf{r})$. The generalization to the vector potential for multiple vortices corresponding to Eq. (4) is straightforward, $\mathbf{A}(\mathbf{r}) \to \sum_j \mathbf{A}(\mathbf{r} - \mathbf{R}_j)$.

For numerical simulations, we regularize the continuum model on a two-dimensional square lattice. We set the lattice constant $a = 1$, along with the choice $v = 1$, $\hbar = 1$. The straightforward regularization $\mathcal{H}_0 \to \mathcal{H}_{0,L} = \sum_{\mathbf{k}} \sigma_x \sin k_x + \sigma_y \sin k_y + \sigma_z(-2 + \cos k_x + \cos k_y) - \mu$ can be improved upon replacing $\sin(k) \to \frac{4}{3}\sin(k) - \frac{1}{6}\sin(2k)$ and $\cos(k) \to \frac{4}{3}\cos(k) - \frac{1}{3}\cos(2k)$ which more faithfully approximates the continuum model $\mathcal{H}_0$ around $\mathbf{k} = 0$ by canceling series expansion coefficients of order k_x^3 and k_y^4 at the cost of involving

hoppings along bonds $2a\mathbf{e}_{x,y}$. This will ultimately allow us to choose a large chemical potential ($\mu = 0.6$) for the simulations in the lattice model while still approximating the dispersion of the continuum model at the Fermi level to a satisfactory degree. This in turn yields a small length scale for the Fermi wavelength k_F^{-1} ($\mu = \hbar v k_F$) allowing for tractable overall system sizes. In real space, the lattice Hamiltonian reads

$$\begin{aligned} H_{0,L} = \sum_{\mathbf{r}} & c_{\mathbf{r}}^\dagger[-2\sigma_z - \mu]c_{\mathbf{r}} + c_{\mathbf{r}+\mathbf{e}_\mathbf{x}}^\dagger\left[\frac{4}{3}\times\frac{\sigma_z + i\sigma_x}{2}\right]c_{\mathbf{r}} \\ & + c_{\mathbf{r}+\mathbf{e}_\mathbf{y}}^\dagger\left[\frac{4}{3}\times\frac{\sigma_z + i\sigma_y}{2}\right]c_{\mathbf{r}} \\ & + c_{\mathbf{r}+2\mathbf{e}_\mathbf{x}}^\dagger\left[-\frac{1}{6}\times\frac{2\sigma_z + i\sigma_x}{2}\right]c_{\mathbf{r}} \\ & + c_{\mathbf{r}+2\mathbf{e}_\mathbf{y}}^\dagger\left[-\frac{1}{6}\times\frac{2\sigma_z + i\sigma_y}{2}\right]c_{\mathbf{r}} + \text{H.c.}, \end{aligned} \tag{5}$$

and the BdG Hamiltonian becomes

$$\mathcal{H}_{BdG,L} = \begin{pmatrix} \mathcal{H}_{0,L} & \Delta \\ \Delta^* & -\sigma_y\mathcal{H}_{0,L}^*\sigma_y \end{pmatrix}. \tag{6}$$

The inclusion of magnetic field and vortices in the lattice model is achieved via a discretized version of Eq. (4) and the Peierls substitution for the hopping matrix element from $\mathbf{r}_1$ to $\mathbf{r}_2$ in $H_{0,L}$,

$$t_{\mathbf{r}_2,\mathbf{r}_1} \to t_{\mathbf{r}_2,\mathbf{r}_1}\exp\left(\frac{ie}{\hbar}\int_{\mathbf{r}_1}^{\mathbf{r}_2} d\mathbf{r}\cdot\mathbf{A}(\mathbf{r})\right). \tag{7}$$

In the limit $\lambda \gg a$, the argument of the exponent can be approximated by $i\sum_j \frac{\theta_j(\mathbf{r}_{12})}{2}[1 - \frac{r_j(\mathbf{r}_{12})}{\lambda}K_1(r_j(\mathbf{r}_{12})/\lambda)]$ where $r_j(\mathbf{r}_{12}) \equiv |\mathbf{R}_j - (\mathbf{r}_1 + \mathbf{r}_2)/2|$ is the distance between the vortex j and the midpoint of the bond from $\mathbf{r}_1$ to $\mathbf{r}_2$ and $\theta_j(\mathbf{r}_{1,2})$ is the angle between the connection lines $\mathbf{r}_{1,2} - \mathbf{R}_j$ measured at the vortex position [41].

The MVM wave function for a single vortex in the continuum model reads [36,37]

$$\Psi(r,\phi) \propto \exp\left[-\zeta^{-1}\int_0^r dp\, f(p)\right]\begin{pmatrix} e^{-i\pi/4}J_0(rk_F) \\ e^{+i\pi/4+i\phi}J_1(rk_F) \\ e^{-i\pi/4-i\phi}J_1(rk_F) \\ -e^{+i\pi/4}J_0(rk_F) \end{pmatrix}, \tag{8}$$

where $J_l(x)$ is the Bessel function of the first kind and the decay in radial direction is governed by the Majorana coherence length is $\zeta = \hbar v/\Delta_0$. Here, the effect of the vector potential $\mathbf{A}(\mathbf{r})$ has been neglected as justified for a single vortex if $\lambda \gg \zeta$.

We choose the lattice model parameters as $\mu = 0.6$, $\Delta_0 = 0.2$, $\xi = 2$, $\lambda = 30$, the unit of energy is given by $\hbar v/a = 1$ and the unit of length is $a = 1$. As summarized in Table I, this choice of parameters is motivated by comparison to the experimentally extracted values for $FeTe_xSe_{1-x}$, which are of similar relative size. Only the London penetration length λ of the lattice model, while still being by far the largest length scale, is chosen smaller than what would be appropriate in $FeTe_xSe_{1-x}$ to keep the required lattice sizes tractable. The one-dimensional gapless Majorana mode localized at the open boundaries of the system does not affect the results below due to sufficient distance between vortices and boundary, so that the hybridization between vortex bound states and the edge modes is negligible compared to inter-vortex hybridizations. The LDOS $\rho(\omega)$ [see Eq. (9) below for a definition] of the finite-size lattice model without vortices and averaged in the center region is shown in Fig. 2 and agrees to the expectation from the continuum model. Further, we have checked that the wave function obtained numerically for a single vortex zero mode agrees with the analytic prediction for the MVM in Eq. (8) and that the first excited CdGM-state appears at an energy of order $0.09 \sim \Delta^2/\mu$ as predicted by theory [14,16].

TABLE I. Summary of parameters used for the lattice model simulations and for the experimentally realized material $FeTe_xSe_{1-x}$, $x \simeq 0.55$ as compiled in Ref. [41]. Here, v and μ are the velocity and chemical potential of the Dirac surface Hamiltonian, respectively. For the lattice model, we set $\hbar v = 1$ and $a = 1$ for the lattice constant. The surface state pairing amplitude without vortices is given by Δ_0 while ξ denotes the length scale on which the pairing decays towards vortex cores. The superconducting coherence length is ζ and the London penetration length is denoted by λ.

	$\hbar v$	μ	Δ_0	$k_F = \mu/\hbar v$
Lat. model	1	0.6	0.2	1.66
$FeTe_xSe_{1-x}$	25 meV · nm	5 meV	1.8 meV	0.2/nm
	ξ	$\zeta = \hbar v/\Delta_0$	λ	
Lat. model	2	5	30	
$FeTe_xSe_{1-x}$	4.6 nm	13.9 nm	500 nm	

III. NONLOCAL TRANSPORT

We now consider a transport setup and attach a scanning tunneling microscope (STM) tip "T" as well as a ground contact, see Fig. 1 (contact "C" is to be added at a later stage, see below). For concreteness and to set the stage for the lattice model simulations using the KWANT software package [42], we model the tip "T" as a one-dimensional chain of

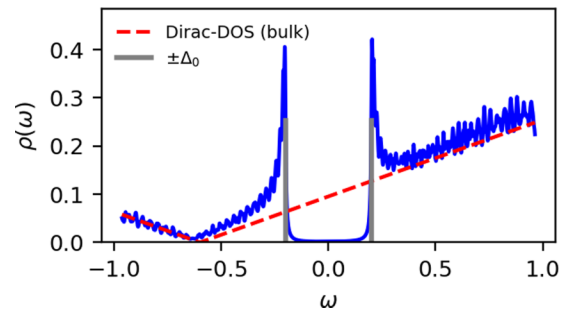

FIG. 2. Tunneling LDOS $\rho(\omega) = \int d\mathbf{r}\rho(\omega,\mathbf{r})/\int d\mathbf{r}$ for the two-dimensional Fu-Kane model in the absence of magnetic field as found from exact diagonalization of the lattice model (6) with parameters $\mu = 0.6$ and $\Delta_0 = 0.2$ and system size $L_x \times L_y = 84\times86$. The oscillations are due to finite-size effects which are incompletely smoothed by the intrinsic level broadening $\Gamma_0 = 0.02\Delta_0 = 0.004$. The superconducting gap $\omega = \pm\Delta_0$ is indicated by grey vertical lines and the density of states (DOS) of the normal-state Dirac Hamiltonian $D(\omega) = \frac{\omega}{2\pi(\hbar v)^2}$ is depicted by the red dashed line.

single sites with hopping $t = 1$ diagonal in spin space. This choice will provide a density of states that does not vary appreciably over the small range of bias $|\omega| \ll 1$ applied in the following. The lead is locally coupled to the surface with hopping γ_T which reflects the tip-sample tunneling matrix element [43] but will be chosen in an *ad hoc* manner below as we are not aiming to model a specific setup. The tip-induced broadening of an eigenstate Φ is $\Gamma_T \equiv \gamma_T^2 n_T/t$ where $n_T \equiv \sum_\sigma |u_\sigma(\mathbf{r}_T)|^2 + |v_\sigma(\mathbf{r}_T)|^2$ is the eigenstate intensity at the lead position.

With the exception of the strong-tunneling experiment by Zhu *et al.* [32], all existing experimental or numerical transport studies of the Fu-Kane setup were done at weak coupling to the tip. This regime is characterized by a tip-induced broadening Γ_T which is smaller than the intrinsic relaxation rate Γ_0 of the quasiparticles. This means that an injected quasiparticle decays in the sample before it can return to the lead. In the case when the intrinsic broadening exceeds the thermal broadening from the leads, $T \lesssim \Gamma_0$ ($k_B = 1$), we obtain the broadened LDOS from [44]

$$\rho(\omega, \mathbf{r}) = \sum_{E_n>0} \frac{\Gamma_0/\pi}{(\omega - E_n)^2 + \Gamma_0^2} \sum_{\sigma=\uparrow,\downarrow} |u_{n,\sigma}(\mathbf{r})|^2 + \sum_{E_n>0} \frac{\Gamma_0/\pi}{(\omega + E_n)^2 + \Gamma_0^2} \sum_{\sigma=\uparrow,\downarrow} |v_{n,\sigma}(\mathbf{r})|^2, \quad (9)$$

where we choose $\Gamma_0 = 0.02\Delta_0 = 0.004$ in Fig. 2 and for the simulations below. The LDOS is proportional to the differential conductance dI/dV at the bias $\omega =$ eV relative to the ground contact, see Fig. 1. In light of Eq. (9), the LDOS yields information about the eigenenergies of the system and the spatial distribution of their wave function's electron and hole content. In particular, it cannot distinguish a MVM at $E_0 = 0$ from an ordinary excitation with energy $E_n > 0$ but smaller than Γ_0 or T.

The experiment of Zhu *et al.* [32] reached the strong coupling regime $\Gamma_T > \Gamma_0$ where quasiparticle transport becomes (approximately) coherent and can be described by a unitary scattering matrix formalism [45]. Due to the bulk superconducting gap, the quasiparticles at subgap energies solely enter and leave through the tip. In the presence of a MVM, perfect Andreev reflection is expected at zero bias which, according to theory [46,47], should yield $G \equiv dI/dV = 2e^2/h$. As this result should be independent of details, a plateau in G as a function of tip-sample separation is expected. It is currently an open question why the experimental conductance plateaus [32] typically show a significantly smaller value for G that varies from vortex to vortex.

We now describe the three-terminal transport setup analyzed in the remainder of this work. We add a second lead ("contact C") at the sample surface in the vicinity of the tip "T", see Fig. 1. We keep the assumption of strong coupling, $\Gamma_{T,C} > \Gamma_0$. At subgap energies $|\omega| \leqslant \Delta_0$, this opens up a multitude of quasiparticle scattering channels where electrons and holes can enter or leave via either lead, provided there is an eigenstate of the isolated sample with simultaneous support at both lead positions. The objects of interest are the (dimensionless) conductances $g_{\alpha\beta} \equiv dI_\alpha/dV_\beta/[e^2/h]$ where I_α is the electrical current flowing into lead $\alpha = \{C, T\}$ and V_β is the bias at lead β. The scattering matrix for this nonlocal setup mediated by a single eigenstate at arbitrary energy E_0 was analyzed by Danon *et al.* [6] for the case of spinless electrons. In the Appendix we generalize this analytical calculation to the case with spin, but the quantitative behavior of the conductances close to the resonance $|\omega| \simeq E_0$ is not affected by this modification. Focusing on equal bias voltage for the two leads, one can approximate the nonlocal zero-temperature conductance as [6]

$$g_{CT}(\omega \simeq \pm E_0) \simeq \frac{-8\xi_C E_0}{\left[\omega^2 - E_0^2\right]^2 + 4\Gamma^2 E_0^2}(E_0\xi_T + \omega\Gamma_T). \quad (10)$$

Here, $\Gamma \equiv \Gamma_C + \Gamma_T$ is the sum over the two lead-induced level broadenings $\Gamma_\alpha \equiv \gamma_\alpha^2 n_\alpha/t$ where $n_\alpha \equiv u_\alpha + v_\alpha$ is the total wave-function intensity at the contact position, with $u_\alpha \equiv \sum_\sigma |u_\sigma(\mathbf{r}_\alpha)|^2$ and $v_\alpha \equiv \sum_\sigma |v_\sigma(\mathbf{r}_\alpha)|^2$. It is assumed that $\Gamma \ll E_0$ for Eq. (10) to hold. The quantity $\xi_\alpha \equiv \gamma_\alpha^2 q_\alpha/t$ is proportional to the local Bardeen-Cooper-Schrieffer (BCS) charge $q_\alpha \equiv u_\alpha - v_\alpha$, which is of central interest in the following discussion. We emphasize that Eq. (10) describes transport mediated by an extended state in the superconducting gap ($E_0 < \Delta$) where transport through the superconducting bulk is suppressed.

The crucial observation in Eq. (10) is the asymmetry of the two peak heights $\omega \simeq \pm E_0$ due to the second term in parenthesis which is odd in ω. We define the symmetric and asymmetric part of the nonlocal conductance as $g_{CT}^{\mathrm{sym/asym}}(\omega) \equiv \frac{1}{2}[g_{CT}(\omega) \pm g_{CT}(-\omega)]$ and observe [6] from Eq. (10)

$$\frac{g_{CT}^{\mathrm{sym}}}{g_{CT}^{\mathrm{asym}}}(\omega \simeq E_0) \simeq \frac{q_T}{n_T} = \frac{|u_T|^2 - |v_T|^2}{|u_T|^2 + |v_T|^2} \in [-1, 1]. \quad (11)$$

This relation allows for the extraction of q_T/n_T, the ratio of BCS charge and intensity of an eigenstate at energy E_0 at the tip position. The prerequisite is that a pair of peaks at $\omega \simeq \pm E_0$ can be identified in the g_{CT} data.

The significance of the quantity q_T/n_T for detecting Majorana zero modes lies in the fact that an isolated Majorana zero mode fulfills $q_T(\mathbf{r}) = 0$ at every position $\mathbf{r}$ due to the particle-hole symmetric nature of the state. On the other hand, for an isolated Majorana zero mode at $E_0 = 0$, the condition $\Gamma \ll E_0$ cannot be achieved. Consequently, one has to rely on the hybridization between zero modes to push the energy E_0 to finite values so that q_T/n_T can be detected by nonlocal transport, thereby compromising $q_T = 0$ to a certain degree. In the following, we apply these general ideas to the case of MVMs and show that MVMs set themselves apart from the CdGM-states at finite energy by a peculiar spatial signature of the q_T/n_T map.

Based on the above discussion and Eq. (10) we discuss the requirements for the second contact "C". While the achievable spatial resolution of q_T/n_T hinges on the sharpness and movability offered by the STM-tip "T", the contact "C" can be stationary. In particular, if no multiple-tip STM instrument is available [33], the contact can even be spatially extended. In light of Eq. (10), such an extended contact will reduce the risk of hitting a contact position where $\xi_C \sim q_C \simeq 0$ which would cause a vanishing nonlocal transport signal. On the other hand, as we require $\Gamma = \Gamma_T + \Gamma_C \ll E_0$ for Eq. (10) to hold in the

first place, we must limit the contact-induced level broadening which grows with contact area and density of states. It might thus be beneficial to choose a contact material with a low density of states, like a graphene flake, or limit the size of the contact using nanofabrication techniques. For example, local gold nanocontacts can be made at selective surface sites using STM via a field-induced atomic emission process *in situ* [48,49]. A discussion on the role of the contact-tip distance is postponed to the end of Sec. V.

We now turn to the leading effect of temperature on the quasiparticle structure, assuming that the temperature remains low enough that the superconducting properties and vortex locations are unmodified. First, the sample temperature T_s needs to be small enough so that the temperature dependent intrinsic quasiparticle decay Γ_0 can be neglected against $\Gamma_{T,C}$ for our coherent nonlocal transport theory to apply. We next consider the effective electron temperature $T_{\mathrm{eff},\alpha}$ in lead α which usually exceeds the sample temperature (Ref. [50] determined 85 mK for the former and about 40 mK for the latter in the case of an STM tip). Theoretically, $T_{\mathrm{eff},\alpha}$ is taken into account by a convolution of $g_{\alpha\beta}(\omega)$ with the derivative of the Fermi function $-\frac{df(\omega,T_{\mathrm{eff},\beta})}{d\omega} = \frac{1}{4T_{\mathrm{eff},\beta}}\cosh^{-2}(\frac{\omega}{2T_{\mathrm{eff},\beta}})$. Since the V_β dependence of I_α is assumed to only enter via the distribution functions of the leads [6], the broadening procedure of g_{CT} in Eq. (10) is to be applied with the effective electron temperature of the tip "T", $T_{\mathrm{eff},T}$. The latter will be abbreviated simply as "temperature" T in the following.

At zero temperature, the peaks of Eq. (10) which occur at $\omega = \pm E_0$ have the same width 2Γ. Hence their temperature broadened amplitudes are diminished simultaneously for both signs of ω. If temperature reaches the scale E_0, the broadening symmetrizes the overall trace $g_{CT}(\omega)$ leading to a underestimation of $|g_{CT}^{\mathrm{asym}}|$ as compared to its $T = 0$ value. As a consequence, the quantity $|g_{CT}^{\mathrm{sym}}/g_{CT}^{\mathrm{asym}}(\omega \simeq E_0)|$ can then exceed unity in magnitude which should be taken as a warning that the right-hand side of Eq. (11) no longer applies.

In the following we theoretically implement the above protocol. We assume that Γ_0 is sufficiently small so that the scattering matrix approach is justified. However, we take into account a finite temperature in the leads. While the case with two vortices studied in the subsequent Sec. IV is still analytically tractable, our numerical approach is particularly useful for the realistic case of a distorted vortex lattice. Here the above assumption of a single spectrally isolated subgap state at energy E_0 drastically fails as every pair of MVMs contributes one fermionic state that cluster in a MVM or CdGM band. However, our exact numerics still shows that the peculiar signatures found for the vortex pair still survive in the vortex lattice $g_{CT}^{\mathrm{sym}}/g_{CT}^{\mathrm{asym}}$ map.

IV. VORTEX PAIR

We now investigate the case of a single pair of vortices where for the hybridized MVMs, we can find $[q/n](\mathbf{r})$ analytically from the single MVM wave function, Eq. (8). We place the vortices at positions $\mathbf{R}_{1,2} = \mathbf{R}_0 \pm R/2\mathbf{e}_x$ and use two sets of polar coordinates $r_j = |\mathbf{r} - \mathbf{R}_j|$ and $\phi_j = \arg(\mathbf{r} - \mathbf{R}_j)$ for $j = 1, 2$. The hybridized MVM states [37] can be approximated by $\Psi_{s=\pm} = (\Psi_1 + si\Psi_2)/\sqrt{2}$ where the phase of the pairing field Δ just left to each vortex is $\Omega_1 = 0$ and $\Omega_2 = \pi$, which is taken into account by a relative prefactor $e^{i\tau_z\Omega_j/2}$ between Ψ_j and Eq. (8). Dropping the wave-function normalization, we obtain for the profile of the intensity and charge density

$$n_s(\mathbf{r}) \propto e^{-2r_1/\zeta}\left[J_0^2(r_1k_F) + J_1^2(r_1k_F)\right] + r_1 \to r_2, \quad (12)$$

$$q_s(\mathbf{r}) \propto -2se^{-(r_1+r_2)/\zeta}\{J_0(r_2k_F)J_0(r_1k_F) + \cos(\phi_1 - \phi_2)J_1(r_1k_F)J_1(r_2k_F)\}. \quad (13)$$

Note that $n_s(\mathbf{r})$ is proportional to sum of the two individual MVM's intensities, qualitatively similar to the LDOS $\rho(\omega, \mathbf{r})$, see Figs. 3(a) and 3(b), for the corresponding plots based on exact diagonalization (ED) of the lattice model. In contrast, the spatial structure of $q_s(\mathbf{r})$ is dominated by the exponential prefactor which gives rise to an ellipsoidal structure with the two vortices in the focal points and oscillations caused by the remaining terms.

We expand the Bessel functions at a sufficient distance from the vortices $r_{1,2}k_F \gg 1$. We further restrict to a point $\mathbf{r}_c$ on the connecting line between the vortices, where $\phi_1 = \pi$, $\phi_2 = 0$, $r_1 + r_2 = R$ and obtain

$$\frac{q_s}{n_s}(\mathbf{r}_c) = \frac{-2se^{-R/\zeta}\frac{1}{\sqrt{r_1r_2}}\sin(k_FR)}{\frac{1}{r_1}\exp(-2r_1/\zeta) + \frac{1}{r_2}\exp(-2r_2/\zeta)}, \quad (14)$$

which is peaked at the mid-point $\bar{\mathbf{r}}_c = (\mathbf{R}_1 + \mathbf{R}_2)/2$. The peak value is $q_s/n_s(\bar{\mathbf{r}}_c) = -s\sin(k_FR)$ which oscillates like the MVM hybridization [37] $E_0 \sim \cos[k_FR + \frac{1}{2}\tan^{-1}(\zeta k_F)]$ with a relative phase shift depending on the value of ζk_F and valid for $R \gg \xi, 1/k_F$. Note that for the theoretically interesting case of $\mu = 0$, which is unrealistic in current materials, chiral symmetry prevents hybridization ($E_0 = 0$) for vortices of the same vorticity [37]. For the lattice model with vortex distance $R = 13$ and $\mu = 0.6$, we present $q_s(\mathbf{r})$ and $[q_s/n_s](\mathbf{r})$ of the hybridized MVM state with $E_0 = 0.0045$ in Fig. 3(c,d). The data for q_s/n_s on the cut between the two vortices is depicted in Fig. 4 (left) and shows good qualitative agreement with the analytical prediction above. A quantitative comparison is complicated due to an inaccuracy of the ansatz $\Psi_{s=\pm} = (\Psi_1 + si\Psi_2)/\sqrt{2}$ as documented by a slight renormalization of the wave-function peak-intensity separation beyond the vortex distance R (data not shown). We remark that in one-dimensional proximitized semiconductor quantum wires a pair of hybridized Majorana bound states is expected to cause a qualitatively similar form for the fraction $\frac{q_s}{n_s}(x)$ [6,51].

We now discuss the numerical lattice-model ED results for ρ, n, q and q/n as obtained for one of the two hybridized first excited states of each vortex which are split around $E \simeq 0.1$, see Figs. 3(e)–3(h) and Fig. 4 (right). While the spatial structure of ρ and n are qualitatively indistinguishable from the MVM case, $q(\mathbf{r})$ shows local maxima around the two vortex positions with radially oscillating signs. This resembles the sum of $q(\mathbf{r})$ of the solutions individual to each vortex. Note that the structures of q/n at larger distances from the vortices shown in Figs. 3(d) and 3(h) emerge from the ratio of two numbers very small in magnitude and are likely unobservable in a nonlocal transport experiment due to insufficient peak visibility and intrinsic broadening, c.f. Eq. (10).

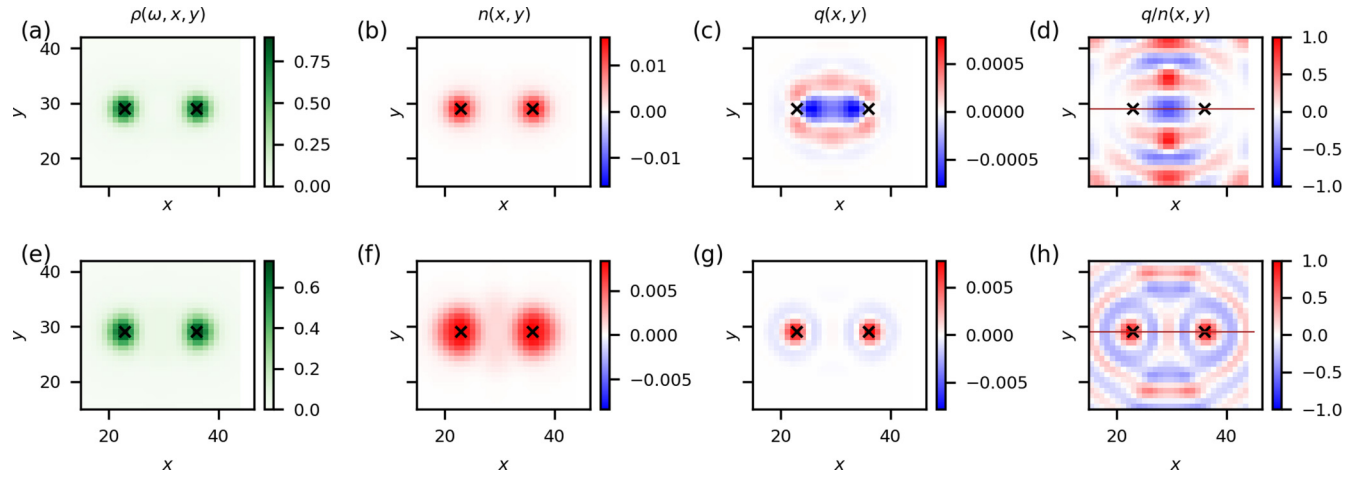

FIG. 3. Numerical lattice-model results from exact diagonalization for a pair of vortices located at a distance $R = 13$ as indicated by the black crosses. The parameters are $\mu = 0.6$, $\Delta_0 = 0.2$, $\xi = 2$ and $\lambda = 30$ and the overall system size is $L_x \times L_y = 60 \times 58$. The top row shows the LDOS ρ [Eq. (9) with $\Gamma_0 = 0.004$, $\omega = E_0$] in panel (a), intensity n in panel (b), charge q in panel (c) and the ratio q/n in panel (d) for the hybridized MVM state at energy $E_0 = 0.0045$, the bottom row with panels (e)–(h) reports the same quantities for the lower one of the two hybridized CdGM-state energies, $E_1 = 0.09$.

In summary, based on the elementary case of a vortex pair, we propose to identify hybridized states of MVMs by their nonlocal spatial distribution of q/n which attains values close to zero at the vortex positions and magnitudes attaining their maxima in between. In contrast, ordinary CdGM states show peaks of $|q/n|$ at the vortex positions. The positions of the vortices can be experimentally obtained from the LDOS $\rho(\omega, \mathbf{r})$ map as usual [19], while the information on q/n can be obtained experimentally from the nonlocal transport measurement via $g_{CT}^{\text{sym}}/g_{CT}^{\text{asym}}$ at an energy $\omega = E_0$ where g_{CT} peaks. While this relation could be shown analytically for the case of a single energetically well-separated subgap state (i.e., the vortex-pair case), it remains valid qualitatively for the case of a band of subgap states as in the case of a distorted vortex lattice as we show below.

In the remainder of this paper, we will demonstrate the above assertion using a numerical implementation of the nonlocal transport measurement on a faithful lattice model with finite-temperature leads attached. We start with the vortex pair, see Fig. 5. The contact "C" is placed at the top boundary of the field of view, in the vicinity of the vortices (green patch). In panel (d) we show the resulting $g_{CT}(\omega, \mathbf{R}_1)$ at the position of the right vortex, panel (a) zooms into small energies. The non-local conductance shows temperature broadened peaks and dips at $|\omega| = E_0 = 0.0045$ and $|\omega| = E_1 = 0.09$ indicating the energies of the hybridized MVM- and CdGM-states in agreement with the ED results [see dashed vertical lines in panels (a) and (d)]. Panels (b) and (e) show a spatial map of $g_{CT}(\omega = E_{0,1}, \mathbf{r})$, respectively. The ratio $g_{CT}^{\text{sym}}/g_{CT}^{\text{asym}}(\omega = E_{0,1})$ for both peak positions is shown in Figs. 5(c) and 5(f), respectively. The agreement with the ED results in Fig. 3 is excellent in almost the entire field of view, confirming the practical applicability of Eq. (11).

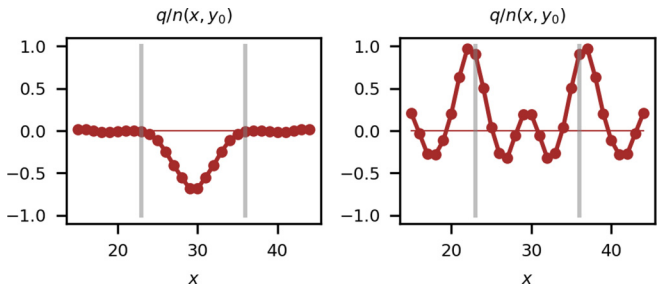

FIG. 4. One-dimensional cut through the data depicted in Figs. 3(d) and 3(h) along the brown line connecting the two vortices. The vertical lines denote the vortex positions. The low energy MVM data from Fig. 3(d) is shown in the left panel, the right panel displays the hybridized finite energy CdGM-state from Fig. 3(h).

V. DISTORTED VORTEX LATTICE

We now turn to the experimentally realistic case of a distorted vortex lattice. Owing to the presence of a finite density of states both in the MVM and CdGM band, the analytical treatment from Sec. III building on the presence of a single spectrally isolated eigenstate *a priori* does not apply any longer and we resort to numerical simulations. We use a large sample $L_x \times L_y = 160 \times 162$ with an average vortex distance $R \sim 13$ similar to the separation of the vortex pair studied above. To avoid edge effects, we focus on the central region of the sample. In Fig. 6, the vortex positions in the central region (which could be found experimentally via the LDOS ρ) are denoted by crosses. The contact (green patch) is placed on the bottom right relative to the scanning-tip field of view which includes 13 vortices (colored crosses). The data for $g_{CT}(\omega, \mathbf{R}_j)$ at these vortex positions are shown in panel (d) and panel (a) shows a zoom-in about low energies where the hybridized MVMs occur. We observe a peak structure at $|\omega| \simeq E_0 = 0.0055$ for the outer ten out of the 13 vortex positions and at $|\omega| \simeq E_1 = 0.105$ for all vortex positions in the field of view. Panels (b) and (e) show the spatially resolved $g_{CT}(\omega, \mathbf{r})$ for $\omega = E_{0,1}$, respectively. Our main result is shown in panels (c) and (f). Here we report $g_{CT}^{\text{sym}}/g_{CT}^{\text{asym}}(\omega = E_{0,1})$ which qualitatively resembles the observations made for the

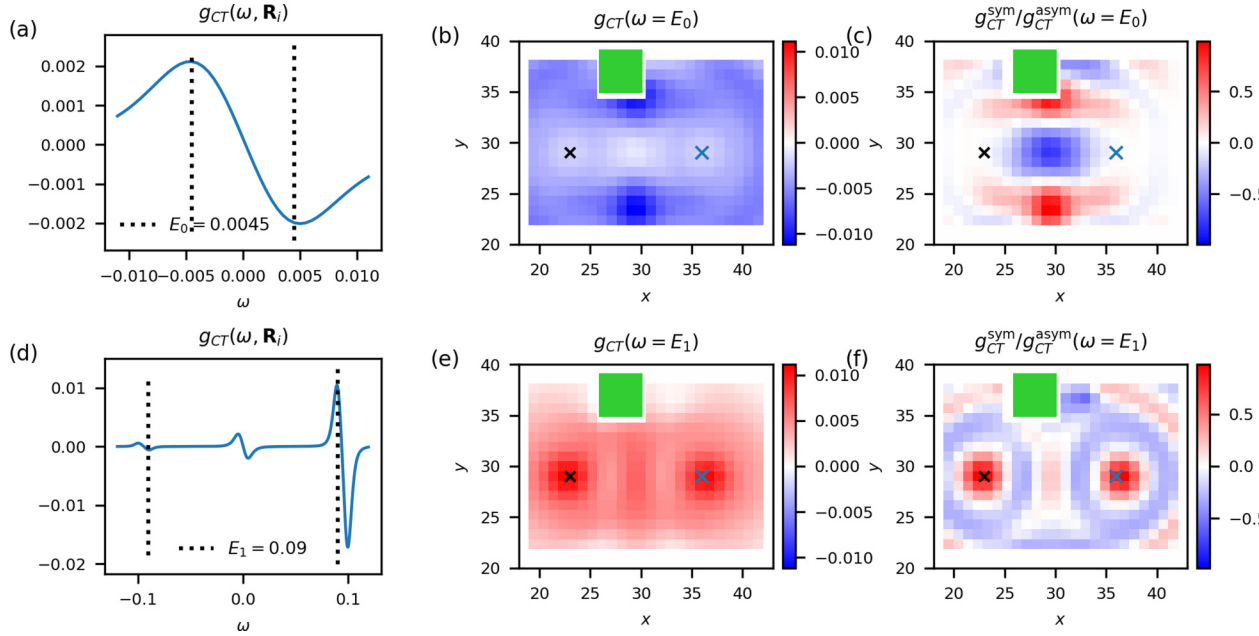

FIG. 5. Nonlocal transport simulation for a lattice model including a vortex pair. We model the tip "T" as a single-atomic lead with $t = 1$ and $\gamma_T = 0.4$ and the extended contact "C" as a $A_C = 4\times4$ patch of the same single-atomic leads with $\gamma_C = 0.1$ (green). For a local intensity n_C on the order of 0.01 (c.f. Fig. 3) this results in a broadening $\Gamma_C = n_C A_C \gamma_C^2/t \simeq 0.002$ which is smaller than the MVM hybridization energy (we neglect the intrinsic broadening Γ_0 in order to obtain a unitary scattering matrix). For the temperature of the leads, we take $T = 0.002$. The model parameters (see Table I) are the same as in Fig. 3. The left column with panels (a), (d) shows the bias-dependent nonlocal conductance $g_{CT}(\omega, \mathbf{R}_1)$ with the tip positioned at the right vortex. A low-energy peak structure highlighted by the vertical dashed lines appears at $|\omega| = E_0 = 0.0045$, see panel (a), and $|\omega| = E_1 = 0.09$, see panel (d). In panels (b) and (e), we depict $g_{CT}(\omega = E_{0,1}, \mathbf{r})$. The right panels (c) and (f) depict $g_{CT}^{\mathrm{sym}}/g_{CT}^{\mathrm{asym}}(\omega = E_{0,1})$, which quantitatively agree to the q/n maps of Figs. 3(d), 3(h).

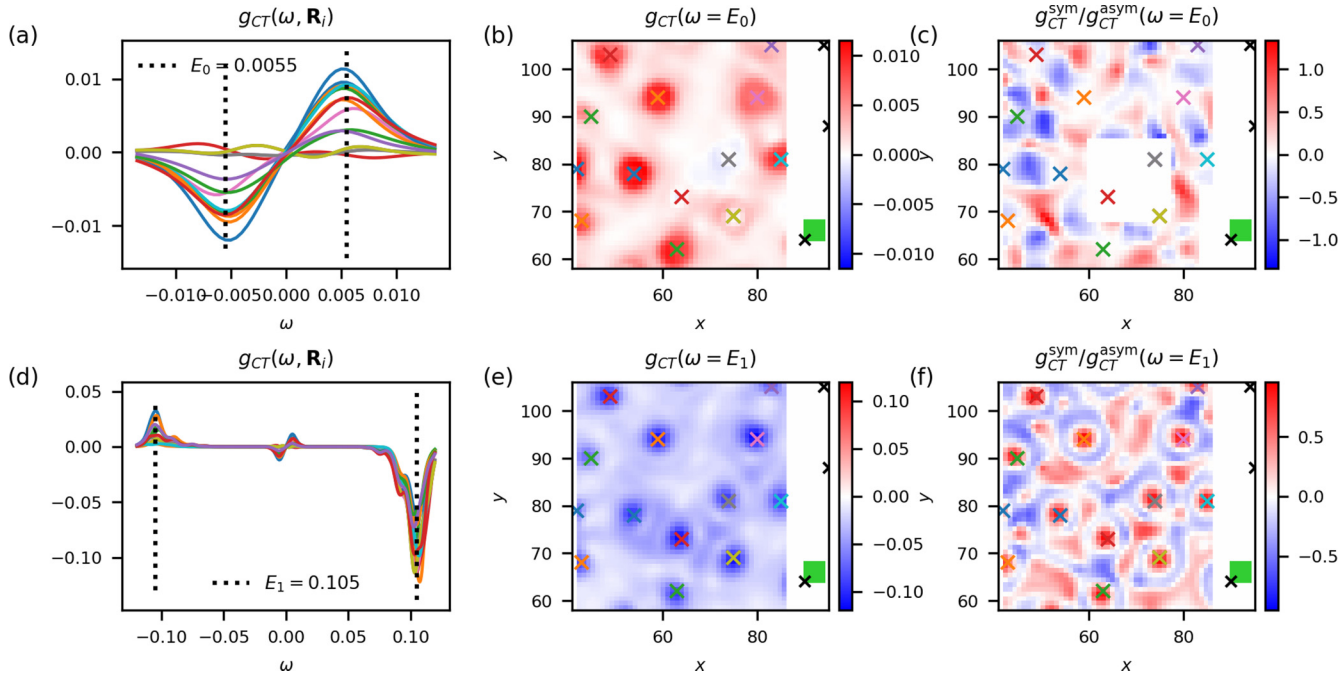

FIG. 6. Nonlocal transport simulation for a lattice model including a set of vortices arranged in a distorted lattice. The parameters are the same as in Fig. 5. The left column with panels (a), (d) shows the bias-dependent nonlocal conductance $g_{CT}(\omega, \mathbf{R}_i)$ for 13 vortices $i = 1, 2, \ldots, 13$. The colors of the lines correspond to the color of the crosses in the other panels, the latter mark the vortex positions. Panel (a) zooms to small bias voltages around the peak at $E_0 = 0.0055$ while panel (d) shows a larger bias range including the peak at $E_1 = 0.105$. In panels (b) and (e), we depict $g_{CT}(\omega, \mathbf{r})$ for $\omega = E_0$ and $\omega = E_1$, respectively. The right panels (c) and (f) depict $g_{CT}^{\mathrm{sym}}/g_{CT}^{\mathrm{asym}}$ for $\omega = E_0$ and $\omega = E_1$, respectively. As the inner three vortices (red, grey, yellow) do not show a pronounced peak structure at low energies $\sim E_0$ in panels (a), (b), we discard their vicinity for the plot in panel (c).

vortex pair: For the MVM band around $\omega = E_0$, the data in panel (c) vanishes at and around the ten outer vortex positions and shows extended nonlocal features in between vortices. We disregard the region around the three central vortices for which no sizable peak structure was observed in the first place. Presumably, the reason for the local absence of sizable peaks is that the MVM band does not contain a state simultaneously supported in the region of the central three vortices and at the contact "C".

The signatures of $g_{CT}^{\mathrm{sym}}/g_{CT}^{\mathrm{asym}}(\omega = E_1)$ at the CdGM-state energy shown in panel (f) are radially symmetric local maxima at all vortex positions with an oscillating behavior in between vortices.

For an experimental realization, the question about the maximally feasible distance between the tip "T" and contact "C" is highly relevant. At this point, the local nature of the intrinsic broadening Γ_0 neglected beyond Eq. (9) will come into play. It violates the assumption of a perfectly coherent subgap state and we expect it to add to the lead-induced broadening Γ in the denominator of the non-local conductance g_{CT} of Eq. (10) and cause a damping of the nonlocal conductance peaks. A detailed numerical modeling of the associated crossover to purely local conductance in Eq. (9) would require the addition of a spatially distributed self-energy term in the simulation which is beyond the scope of this paper (and the state-of-the-art). However, we anticipate that the modification of the g_{CT} signal should not compromise the peak-height ratios and the assessment of q/n until the effective broadening reaches the scale E_0, compare to the discussion of temperature effects in the leads at the end of Sec. III.

Another aspect is a possible (single-particle) Anderson localization [52] in the band of MVM states, which would limit the tip-contact separation to the localization length. However, the two-dimensional Majorana-only model (symmetry class D) is known to feature weak-antilocalization and thus hosts both a localized Anderson insulating phase and a delocalized "thermal" metal phase, with a phase diagram that is largely unknown. What has been studied is the transition from a regular triangular Majorana lattice with uniform $\pi/2$ flux through each triangular plaquette (a topological band insulator) to the thermal metal phase which occurs when a randomly chosen minority of $\sim$15% of hopping terms have their signs flipped [53]. Since the signs of the mutual MVM hopping terms are known to oscillate [37] with k_F^{-1} which is on the order of the spread in the intervortex distances, we believe that the realistic systems are well in the thermal metal phase. However, more detailed studies, preferably performed in a Majorana-only effective model [54] are desirable.

VI. CONCLUSION

We proposed to apply a nonlocal quantum transport measurement to identify the presence (or absence) of hybridized Majorana zero modes in the vortex cores in Fu-Kane materials, like the surface of iron-based superconductors. In contrast to recent applications of this method to one-dimensional "Majorana" wires [6,9], the spatial resolution inherent in the putative two-dimensional Majorana platforms allows us to extract telltale spatial signatures of MVM or CdGM states from the symmetry properties of the peaks in the nonlocal conductance trace, see Eq. (11). We first treated the case of a vortex pair analytically and confirmed our findings using transport simulations based on a lattice model. Finally, we showed that the proposed signatures persist in the experimentally relevant case of a distorted lattice model.

We emphasize that the presented features in the ratio q/n are generic. The only requirement is a sufficiently large hybridization E_0, a value that oscillates with separation R in the two-vortex case. If E_0 approaches zero as a matter of fine-tuning, the nonlocal conductance peaks move towards zero-bias and will not be observable such that the experimental protocol cannot be implemented for that particular state. This suggests that there is no danger in a false-positive identification of MVM. Further evidence for this also comes from the vortex-lattice case in Fig. 6(c), where, despite the random (and certainly not fine-tuned) placement of more than ten vortices, the features in question remain clearly distinct. For other perturbations beyond our model (e.g., disorder potentials), the stability of the proposed signatures remains to be explored.

We expect our results to be relevant for all existing platforms of candidate Fu-Kane materials showing signatures of putative MVMs, see Sec. I. Moreover, our proposal should be applicable to recently suggested alternative realizations of MVMs, like giant topological vortices trapped in an ordinary superconductors with a dislocation line [55]. For future work, it would be interesting to extend our nonlocal transport proposal to spin-polarized or superconducting leads [56] or to consider the case of a non-negligible intrinsic level broadening [57].

ACKNOWLEDGMENTS

We acknowledge useful discussions with K. Flensberg. Computations were performed at the Lawrencium cluster at Lawrence Berkeley National Lab. B.S., A-P.L., M.B., R.G.M., and J.E.M. acknowledge support by the U.S. Department of Energy (DOE), Office of Science, National Quantum Information Science Research Centers, the Quantum Science Center (QSC), a National Quantum Information Science Research Center of the U.S. Department of Energy (DOE). B.S. acknowledges financial support by the German National Academy of Sciences Leopoldina through Grants No. LPDS 2018-12 and No. LPDR 2021-01. M.G. acknowledges support by the European Research Council (ERC) under the European Union' s Horizon 2020 research and innovation program under Grant Agreement No. No.˜856526, and from the Deutsche Forschungsgemeinschaft (DFG) project Grant No. 277101999 within the CRC network TR 183 (subProject No. C01), and from the Danish National Research Foundation, the Danish Council for Independent Research | Natural Sciences.

APPENDIX: SPINFUL SCATTERING MATRIX FOR TWO NORMAL LEADS COUPLED TO A SUBGAP STATE AT ENERGY E_0

We start from the general expression of the scattering matrix [58]

$$S(\omega) = 1 - \frac{2i}{t} H_{LS} \frac{1}{\omega - H_S + \frac{i}{t} H_{SL} H_{LS}} H_{SL}, \tag{A1}$$

TABLE II. Summary of abbreviations used in the analytical calculation in the Appendix.

$\lvert u_\alpha\rvert^2 \equiv \sum_\sigma \lvert u_{\alpha,\sigma}\rvert^2$	$n_\alpha \equiv \lvert u_\alpha\rvert^2 + \lvert v_\alpha\rvert^2$	$\Gamma_\alpha \equiv \frac{\gamma_\alpha^2}{t} n_\alpha$	$\Gamma \equiv \Gamma_L + \Gamma_R$
$\lvert v_\alpha\rvert^2 \equiv \sum_\sigma \lvert v_{\alpha,\sigma}\rvert^2$	$q_\alpha \equiv \lvert u_\alpha\rvert^2 - \lvert v_\alpha\rvert^2$	$\xi_\alpha \equiv \frac{\gamma_\alpha^2}{t} q_\alpha$	$\xi^2 \equiv \xi_L^2 + \xi_R^2$
$[uv]_\alpha \equiv \sum_\sigma u_{\sigma\alpha} v_{\sigma\alpha}$	$\Xi_\alpha \equiv \gamma_\alpha^4 \lvert[uv]_\alpha\rvert^2$	$4\lvert u_\alpha\rvert^2\lvert v_\alpha\rvert^2 = n_\alpha^2 - q_\alpha^2$	$\xi_{LR}^2 = \frac{1}{t^2}\gamma_L^2\gamma_R^2([uv]_R)^\star[uv]_L$
$a \equiv 2\gamma_L^2[uv]_L + 2\gamma_R^2[uv]_R$	$\lvert a\rvert^2 = 8\mathrm{Re}\xi_{LR}^2 + 4\Xi_L + 4\Xi_R$	$b_\pm \equiv \omega \pm E_0 + i\Gamma$	$c \equiv \omega^2 - \Gamma^2 - E_0^2 + \lvert a\rvert^2$

which assumes normal (nonsuperconducting) leads with hopping t. It can be derived from the Fisher-Lee relation which is more complicated due to one additional matrix inversion. Here, H_S is the Hamiltonian of scattering region to which the leads are coupled with $H_{LS} = H_{SL}^\dagger$.

We now focus on a superconducting system in BdG formulation and limit ourselves to a single particle-hole symmetric pair of eigenstates, $H_S\Phi = E_0\Phi$ and $H_S(P\Phi) = -E_0(P\Phi)$. We insert into Eq. (A1) and find

$$S(\omega) = 1 - \frac{2i}{t} W^\dagger \frac{1}{\begin{pmatrix} \omega - E_0 & 0 \\ 0 & \omega + E_0 \end{pmatrix} + \frac{i}{t} WW^\dagger} W, \tag{A2}$$

$$W \equiv \begin{pmatrix} \Phi^\dagger \\ (P\Phi)^\dagger \end{pmatrix} H_{SL}. \tag{A3}$$

We further assume a set of leads such that H_{SL} is diagonal in the lead index α. For lead α, we have in the BdG formulation $H_{SL}^\alpha = \gamma_\alpha \tau_z$ with $\gamma_\alpha \in \mathbb{R}$ a spin-independent hopping.

For the spinless case, we can chose $\Phi = (u^\star, v)^{\mathrm{T}}$ and with $\mathcal{P} = \tau_x\mathcal{K}$ we find

$$W_\alpha = \gamma_\alpha \begin{pmatrix} u_\alpha & -v_\alpha^\star \\ v_\alpha & -u_\alpha^\star \end{pmatrix}, \tag{A4}$$

where $u_\alpha = u(\mathbf{r}_\alpha)$ is the electron part of the BdG wave function at the position of lead α and similar for the hole-part v_α. For the spinless case and in the presence of two leads $\alpha = \{L, R\}$, Ref. [6] derived an explicit expression for the scattering matrix and conductances.

We now generalize the calculation for the spinful case where $\Phi = (u_\uparrow, u_\downarrow, v_\downarrow, -v_\uparrow)$ and $\mathcal{P} = \sigma_y\tau_y\mathcal{K}$. In this case, we obtain

$$W_\alpha = \gamma_\alpha \begin{pmatrix} u_{\uparrow,\alpha}^\star & u_{\downarrow,\alpha}^\star & -v_{\downarrow,\alpha}^\star & v_{\uparrow,\alpha}^\star \\ v_{\uparrow,\alpha} & v_{\downarrow,\alpha} & -u_{\downarrow,\alpha} & u_{\uparrow,\alpha} \end{pmatrix}. \tag{A5}$$

We set $t \equiv 1$ in the following and use the definitions and relations in Table II some of which already appeared in the main text. We find

$$iWW^\dagger = i\begin{pmatrix} \Gamma & a^\star \\ a & \Gamma \end{pmatrix} \tag{A6}$$

and insert this in Eq. (A2), where $\alpha, \beta = \{L, R\}$:

$$S_{\alpha\beta}(\omega) = \delta_{\alpha\beta} - \frac{2i\gamma_\alpha\gamma_\beta}{c + 2i\Gamma\omega} \begin{pmatrix} u_{\uparrow,\alpha} & v_{\uparrow,\alpha}^\star \\ u_{\downarrow,\alpha} & v_{\downarrow,\alpha}^\star \\ -v_{\downarrow,\alpha} & -u_{\downarrow,\alpha}^\star \\ v_{\uparrow,\alpha} & u_{\uparrow,\alpha}^\star \end{pmatrix} \times \begin{pmatrix} b_+ & -ia^\star \\ -ia & b_- \end{pmatrix} \begin{pmatrix} u_{\uparrow,\beta}^\star & u_{\downarrow,\beta}^\star & -v_{\downarrow,\beta}^\star & v_{\uparrow,\beta}^\star \\ v_{\uparrow,\beta} & v_{\downarrow,\beta} & -u_{\downarrow,\beta} & u_{\uparrow,\beta} \end{pmatrix}. \tag{A7}$$

We now extract the submatrices required for computing the local and nonlocal conductance, g_{LL} and g_{LR}:

$$g_{LL} = N_L - \mathrm{tr}[s_{ee,LL}^\dagger s_{ee,LL}] + \mathrm{tr}[s_{he,LL}^\dagger s_{he,LL}], \tag{A8}$$

$$g_{LR} = -\mathrm{tr}[s_{ee,LR}^\dagger s_{ee,LR}] + \mathrm{tr}[s_{he,LR}^\dagger s_{he,LR}]. \tag{A9}$$

After straightforward but lengthy algebra, we obtain

$$g_{LL}(\omega) = \frac{4}{|c + 2i\Gamma\omega|^2}\big[4c\big(\Xi_L + \mathrm{Re}\big[\xi_{LR}^2\big]\big) + \big(\Gamma\Gamma_L - \xi_L^2\big)(2\omega^2 - c) + \omega\xi_L\big\{2\Gamma_R E_0 - 8\mathrm{Im}\big[\xi_{LR}^2\big]\big\}\big], \tag{A10}$$

$$g_{LR}(\omega) = \frac{4\xi_L}{|c - 2i\Gamma\omega|^2}\big\{\xi_R(c - 2\omega^2) - \omega\big(2\Gamma_R E_0 - 8\mathrm{Im}\xi_{LR}^2\big)\big\}. \tag{A11}$$

In the main text, we are only interested in $g_{LR}(\omega)$. We obtain Eq. (10) for $|\omega| \simeq E_0$ assuming that E_0 is much larger than all other scales appearing in Eq. (A11).

[1] J. Alicea, New directions in the pursuit of Majorana fermions in solid state systems, Rep. Prog. Phys. **75**, 076501 (2012).

[2] J. Sau and S. Tewari, From Majorana fermions to topological quantum computation in semiconductor/superconductor heterostructures, arXiv:2105.03769.

[3] V. Mourik, K. Zuo, S. M. Frolov, S. R. Plissard, E. P. A. M. A. M. Bakkers, and L. P. Kouwenhoven, Signatures of majorana fermions in hybrid superconductor-semiconductor nanowire devices, Science **336**, 1003 (2012).

[4] H. Zhang, C. X. Liu, S. Gazibegovic *et al.*, Retraction Note: Quantized Majorana conductance, Nature **591**, E30 (2021).

[5] T. O. Rosdahl, A. Vuik, M. Kjaergaard, and A. R. Akhmerov, Andreev rectifier: A nonlocal conductance signature of topological phase transitions, Phys. Rev. B **97**, 045421 (2018).

[6] J. Danon, A. B. Hellenes, E. B. Hansen, L. Casparis, A. P. Higginbotham, and K. Flensberg, Nonlocal Conductance Spectroscopy of Andreev Bound States: Symmetry Relations and BCS Charges, Phys. Rev. Lett. **124**, 036801 (2020).

[7] H. Pan, J. D. Sau, and S. Das Sarma, Three-terminal nonlocal conductance in majorana nanowires: Distinguishing topological and trivial in realistic systems with disorder and inhomogeneous potential, Phys. Rev. B **103**, 014513 (2021).

[8] D. I. Pikulin, B. van Heck, T. Karzig, E. A. Martinez, B. Nijholt, T. Laeven, G. W. Winkler, J. D. Watson, S. Heedt, M. Temurhan, V. Svidenko, R. M. Lutchyn, M. Thomas, G. de Lange, L. Casparis, and C. Nayak, Protocol to identify a topological superconducting phase in a three-terminal device, arXiv:2103.12217.

[9] G. C. Ménard, G. L.R. Anselmetti, E. A. Martinez, D. Puglia, F. K. Malinowski, J. S. Lee, S. Choi, M. Pendharkar, C. J. Palmstrøm, K. Flensberg, C. M. Marcus, L. Casparis, and A. P. Higginbotham, Conductance-Matrix Symmetries of a Three-Terminal Hybrid Device, Phys. Rev. Lett. **124**, 036802 (2020).

[10] D. Puglia, E. A. Martinez, G. C. Ménard, A. Pöschl, S. Gronin, G. C. Gardner, R. Kallaher, M. J. Manfra, C. M. Marcus, A. P. Higginbotham, and L. Casparis, Closing of the induced gap in a hybrid superconductor-semiconductor nanowire, Phys. Rev. B **103**, 235201 (2021).

[11] L. Fu and C. L. Kane, Superconducting Proximity Effect and Majorana Fermions at the Surface of a Topological Insulator, Phys. Rev. Lett. **100**, 096407 (2008).

[12] J. P. Xu, M. X. Wang, Z. L. Liu, J. F. Ge, X. Yang, C. Liu, Z. A. Xu, D. Guan, C. L. Gao, D. Qian, Y. Liu, Q. H. Wang, F. C. Zhang, Q. K. Xue, and J. F. Jia, Experimental Detection of a Majorana Mode in the Core of a Magnetic Vortex inside a Topological Insulator-Superconductor $Bi_2Te_3/NbSe_2$ Heterostructure, Phys. Rev. Lett. **114**, 017001 (2015).

[13] H. H. Sun, K. W. Zhang, L. H. Hu, C. Li, G. Y. Wang, H. Y. Ma, Z. A. Xu, C. L. Gao, D. D. Guan, Y. Y. Li, C. Liu, D. Qian, Y. Zhou, L. Fu, S. C. Li, F. C. Zhang, and J. F. Jia, Majorana Zero Mode Detected with Spin Selective Andreev Reflection in the Vortex of a Topological Superconductor, Phys. Rev. Lett. **116**, 257003 (2016).

[14] C. Caroli, P. G. De Gennes, and J. Matricon, Bound Fermion states on a vortex line in a type II superconductor, Phys. Lett. **9**, 307 (1964).

[15] G. E. Volovik, Fermion zero modes on vortices in chiral superconductors, JETP Lett. **70**, 609 (1999).

[16] I. M. Khaymovich, N. B. Kopnin, A. S. Mel'Nikov, and I. A. Shereshevskii, Vortex core states in superconducting graphene, Phys. Rev. B **79**, 224506 (2009).

[17] L. Kong, S. Zhu, M. Papaj, H. Chen, L. Cao, H. Isobe, Y. Xing, W. Liu, D. Wang, P. Fan, Y. Sun, S. Du, J. Schneeloch, R. Zhong, G. Gu, L. Fu, H. J. Gao, and H. Ding, Half-integer level shift of vortex bound states in an iron-based superconductor, Nat. Phys. **15**, 1181 (2019).

[18] D. Wang, L. Kong, P. Fan, H. Chen, S. Zhu, W. Liu, L. Cao, Y. Sun, S. Du, J. Schneeloch, R. Zhong, G. Gu, L. Fu, H. Ding, and H. J. Gao, Evidence for Majorana bound states in an iron-based superconductor, Science **362**, 333 (2018).

[19] T. Machida, Y. Sun, S. Pyon, S. Takeda, Y. Kohsaka, T. Hanaguri, T. Sasagawa, and T. Tamegai, Zero-energy vortex bound state in the superconducting topological surface state of Fe(Se,Te), Nat. Mater. **18**, 811 (2019).

[20] D. Wang, R. Zhong, G. Gu, and R. Wiesendanger, Surface orbital order and chemical potential inhomogeneity of the iron-based superconductor $Fete_{0.55}se_{0.45}$ investigated with special stm tips, Phys. Rev. Research **3**, L032055 (2021).

[21] P. Zhang, Z. Wang, X. Wu, K. Yaji, Y. Ishida, Y. Kohama, G. Dai, Y. Sun, C. Bareille, K. Kuroda, T. Kondo, K. Okazaki, K. Kindo, X. Wang, C. Jin, J. Hu, R. Thomale, K. Sumida, S. Wu, K. Miyamoto *et al.*, Multiple topological states in iron-based superconductors, Nat. Phys. **15**, 41 (2019).

[22] A. Kreisel, P. J. Hirschfeld, and B. M. Andersen, On the remarkable superconductivity of fese and its close cousins, Symmetry **12**, 1402 (2020).

[23] Q. Liu, C. Chen, T. Zhang, R. Peng, Y.-J. Yan, Ch.-H.-P. Wen, X. Lou, Y.-L. Huang, J.-P. Tian, X.-L. Dong, G.-W. Wang, W.-C. Bao, Q.-H. Wang, Z.-P. Yin, Z.-X. Zhao, and D.-L. Feng, Robust and Clean Majorana Zero Mode in the Vortex Core of High-Temperature Superconductor $(Li_{0.84}Fe_{0.16})$ OHFeSe, Phys. Rev. X **8**, 041056 (2018).

[24] T. T. Zhang, W. C. Bao, C. Chen, D. Li, Z. Lu, Y. Hu, W. Yang, D. Zhao, Y. J. Yan, X. L. Dong, Q. H. Wang, T. T. Zhang, D. L. Feng, Q. Liu, C. Chen, T. T. Zhang, R. Peng, Y. J. Yan, C. H. P. Wen, X. Lou *et al.*, Observation of Distinct Spatial Distributions of the Zero and Nonzero Energy Vortex Modes in $(Li_{0.84}Fe_{0.16})$OHFeSe, Phys. Rev. Lett. **126**, 127001 (2021).

[25] L. Kong, L. Cao, S. Zhu, M. Papaj, G. Dai, G. Li, P. Fan, W. Liu, F. Yang, X. Wang, X. Du, C. Jin, L. Fu, H.-J. Gao, and H. Ding, Majorana zero modes in impurity-assisted vortex of LiFeAs superconductor, Nat. Commun. **12**, 4146 (2021).

[26] W Liu, L. Cao, S. Zhu, L. Kong, G. Wang, M. Papaj, P. Zhang, Y.-B. Liu, H. Chen, G. Li, F. Yang, T. Kondo, S. Du, G.-H. Cao, S. Shin, L. Fu, Z. Yin, H.-J. Gao, and H. Ding, A new Majorana platform in an fe-as bilayer superconductor, Nat. Commun. **11**, 5688 (2020).

[27] Y. Yuan, J. Pan, X. Wang, Y. Fang, C. Song, L. Wang, K. He, X. Ma, H. Zhang, F. Huang, W. Li, and Q. K. Xue, Evidence of anisotropic Majorana bound states in 2M-WS2, Nat. Phys. **15**, 1046 (2019).

[28] Y.W. Li, H.J. Zheng, Y.Q. Fang, D.Q. Zhang, Y.J. Chen, C. Chen, A.J. Liang, W.J. Shi, D. Pei, L.X. Xu, J. Pan, D.H. Lu, M. Hashimoto, A. Barinov, S.W. Jung, C. Cacho, M.X. Wang, Y. He, L. Fu, H.J. Zhang *et al.*, Observation of topological superconductivity in a stoichiometric transition metal dichalcogenide 2m-Ws2, Nat. Commun. **12**, 2874 (2021).

[29] Y. Li, N. Zaki, V. O. Garlea, A. T. Savici, D. Fobes, Z. Xu, F. Camino, C. Petrovic, G. Gu, P. D. Johnson, J. M. Tranquada, and I. A. Zaliznyak, Electronic properties of the bulk and surface states of $Fe_{1+y}Te_{1-x}Se_x$, Nat. Mater. **20**, 1221 (2021).

[30] H. Kim, Y. Nagai, L. Rózsa, D. Schreyer, and R. Wiesendanger, Anisotropic non-split zero-energy vortex bound states in a conventional superconductor, Appl. Phys. Rev. **8**, 031417 (2021).

[31] X. Chen, W. Duan, X. Fan, W. Hong, K. Chen, H. Yang, S. Li, H. Luo, and H.-H. Wen, Friedel Oscillations of Vortex Bound States under Extreme Quantum Limit in $KCa_2Fe_4As_4F_2$, Phys. Rev. Lett. **126**, 257002 (2021).

[32] S. Zhu, L. Kong, L. Cao, H. Chen, Michał Papaj, S. Du, Y. Xing, W. Liu, D. Wang, C. Shen, F. Yang, J. Schneeloch, R. Zhong, G. Gu, L. Fu, Y. Y. Zhang, H. Ding, and H. J. Gao, Nearly quantized conductance plateau of vortex zero mode in an iron-based superconductor, Science **367**, 189 (2020).

[33] A.-P. Li, K. W. Clark, X.-G. Zhang, and A. P. Baddorf, Electron transport at the nanometer-scale spatially revealed by four-probe scanning tunneling microscopy, Adv. Funct. Mater. **23**, 2509 (2013).

[34] K. W. Clark, X.-G. Zhang, I. V. Vlassiouk, G. He, R. M. Feenstra, and A.-P. Li, Spatially resolved mapping of electrical conductivity across individual domain (grain) boundaries in graphene, ACS Nano **7**, 7956 (2013).

[35] K. W. Clark, X.-G. Zhang, G. Gu, J. Park, G. He, R. M. Feenstra, and A.-P. Li, Energy Gap Induced by Friedel Oscillations Manifested as Transport Asymmetry at Monolayer-Bilayer Graphene Boundaries, Phys. Rev. X **4**, 011021 (2014).

[36] M. Cheng, R. M. Lutchyn, V. Galitski, and S. Das Sarma, Splitting of Majorana-Fermion Modes due to Intervortex Tunneling

in a $p_x + ip_y$ Superconductor, Phys. Rev. Lett. **103**, 107001 (2009).

[37] M. Cheng, R. M. Lutchyn, V. Galitski, and S. Das Sarma, Tunneling of anyonic Majorana excitations in topological superconductors, Phys. Rev. B **82**, 094504 (2010).

[38] R. R. Biswas, Majorana Fermions in Vortex Lattices, Phys. Rev. Lett. **111**, 136401 (2013).

[39] T. Liu and M. Franz, Electronic structure of topological superconductors in the presence of a vortex lattice, Phys. Rev. B **92**, 134519 (2015).

[40] We have assumed for simplicity here that the Dirac point is at the Γ point $k = 0$ and that the spin-momentum locking is parallel, neither of which is essential.

[41] C. K. Chiu, T. Machida, Y. Huang, T. Hanaguri, and F. C. Zhang, Scalable Majorana vortex modes in iron-based superconductors, Sci. Adv. **6**, eaay0443 (2020).

[42] C. Groth, M. Wimmer, A. Akhmerov, and X. Waintal, Kwant: a software package for quantum transport, New J. Phys. **16**, 063065 (2014).

[43] J. Tersoff and D. R. Hamann, Theory and Application for the Scanning Tunneling Microscope, Phys. Rev. Lett. **50**, 1998 (1983).

[44] I. Martin and D. Mozyrsky, Nonequilibrium theory of tunneling into a localized state in a superconductor, Phys. Rev. B **90**, 100508(R) (2014).

[45] Y. V. Nazarov and Y. M. Blanter, *Theory of Quantum Transport* (Cambridge University Press, Cambridge, 2009).

[46] K. T. Law, P. A. Lee, and T. K. Ng, Majorana Fermion Induced Resonant Andreev Reflection, Phys. Rev. Lett. **103**, 237001 (2009).

[47] K. Flensberg, Tunneling characteristics of a chain of Majorana bound states, Phys. Rev. B **82**, 180516(R) (2010).

[48] S. Qin, T.-H. Kim, Y. Zhang, W. Ouyang, H. H. Weitering, C.-K. Shih, A. P. Baddorf, R. Wu, and A.-P. Li, Correlating electronic transport to atomic structures in self-assembled quantum wires, Nano Lett. **12**, 938 (2012).

[49] S. Qin, S. Hellstrom, Z. Bao, B. Boyanov, and A.-P. Li, Contacting nanowires and nanotubes with atomic precision for electronic transport, Appl. Phys. Lett. **100**, 103103 (2012).

[50] T. Machida, Y. Kohsaka, and T. Hanaguri, A scanning tunneling microscope for spectroscopic imaging below 90 mK in magnetic fields up to 17.5 T, Rev. Sci. Instrum. **89**, 093707 (2018).

[51] G. Ben-Shach, A. Haim, I. Appelbaum, Y. Oreg, A. Yacoby, and B. I. Halperin, Detecting Majorana modes in one-dimensional wires by charge sensing, Phys. Rev. B **91**, 045403 (2015).

[52] F. Evers and A. D. Mirlin, Anderson transitions, Rev. Mod. Phys. **80**, 1355 (2008).

[53] C. R. Laumann, A. W. W. Ludwig, D. A. Huse, and S. Trebst, Disorder-induced Majorana metal in interacting non-Abelian anyon systems, Phys. Rev. B **85**, 161301(R) (2012).

[54] V. Pathak, S. Plugge, and M. Franz, Majorana bound states in vortex lattices on iron-based superconductors, Ann. Phys. (N.Y.). **435**, 168431 (2021).

[55] S. Rex and R. Willa, A topological flux trap: Majorana bound states at screw dislocations, New J. Phys. **24**, 053057 (2022).

[56] M. Ruby, F. Pientka, Y. Peng, F. Von Oppen, B. W. Heinrich, and K. J. Franke, Tunneling Processes into Localized Subgap States in Superconductors, Phys. Rev. Lett. **115**, 087001 (2015).

[57] C. X. Liu, J. D. Sau, and S. Das Sarma, Role of dissipation in realistic Majorana nanowires, Phys. Rev. B **95**, 054502 (2017).

[58] I. Aleiner, P. Brouwer, and L. Glazman, Quantum effects in Coulomb blockade, Phys. Rep. **358**, 309 (2002).